

Article

Realization of Empathy Capability for the Evolution of Artificial Intelligence Using an MXene(Ti_3C_2)-Based Memristor

Yu Wang ¹, Yanzhong Zhang ¹, Yanji Wang ¹, Hao Zhang ², Xinpeng Wang ², Rongqing Xu ^{1,*} and Yi Tong ^{2,*}

¹ Engineering & College of Flexible Electronics (Future Technology), Nanjing University of Posts and Telecommunications, Nanjing 210023, China; 2020020114@njupt.edu.cn (Y.W.); 1221025009@njupt.edu.cn (Y.Z.); 1021021019@njupt.edu.cn (Y.W.)

² Gusu Lab, Suzhou 215000, China; zhanghao2021@gusulab.ac.cn (H.Z.); wangxinpeng2020@gusulab.ac.cn (X.W.)

* Correspondence: xurq@njupt.edu.cn (R.X.); tongyi@njupt.edu.cn (Y.T.)

Abstract: Empathy is the emotional capacity to feel and understand the emotions experienced by other human beings from within their frame of reference. As a unique psychological faculty, empathy is an important source of motivation to behave altruistically and cooperatively. Although human-like emotion should be a critical component in the construction of artificial intelligence (AI), the discovery of emotional elements such as empathy is subject to complexity and uncertainty. In this work, we demonstrated an interesting electrical device (i.e., an MXene (Ti_3C_2) memristor) and successfully exploited the device to emulate a psychological model of “empathic blame”. To emulate this affective reaction, MXene was introduced into memristive devices because of its interesting structure and ionic capacity. Additionally, depending on several rehearsal repetitions, self-adaptive characteristic of the memristive weights corresponded to different levels of empathy. Moreover, an artificial neural system was designed to analogously realize a moral judgment with empathy. This work may indicate a breakthrough in making cool machines manifest real voltage-motivated feelings at the level of the hardware rather than the algorithm.

Keywords: memristor; MXene; empathy; artificial neuron



Citation: Wang, Y.; Zhang, Y.; Wang, Y.; Zhang, H.; Wang, X.; Xu, R.; Tong, Y. Realization of Empathy Capability for the Evolution of Artificial Intelligence Using an MXene(Ti_3C_2)-Based Memristor.

Electronics **2024**, *13*, 1632.
<https://doi.org/10.3390/electronics13091632>

Academic Editor: Francesco Driussi

Received: 29 March 2024

Revised: 18 April 2024

Accepted: 22 April 2024

Published: 24 April 2024



Copyright: © 2024 by the authors. Licensee MDPI, Basel, Switzerland. This article is an open access article distributed under the terms and conditions of the Creative Commons Attribution (CC BY) license (<https://creativecommons.org/licenses/by/4.0/>).

1. Introduction

Empathy is widely known as an intellectual reaction of one individual to the observed feelings and experiences of another. Of all the ways that we manage interpersonal communication, empathy is among the most humanized and resonant feeling that allows us to develop invaluable interpersonal relationships to the next level (i.e., adult sociability, child discipline, and moral judgments) [1–6]. Humanity dreams of producing computers with human-like capabilities of interpretation and generating empathic features. Recent reports have shown that neuromorphic devices and machine learning can be used to automate facial recognition of positive and negative affections (e.g., angry, excited, and frustrated). D. Qi et al. reported a brain-inspired hierarchical interactive in-memory computing system for video sentiment analysis based on the Ag/a-Carbon/Ag memristor with a structure of 1T1M [7]. However, very few cognitive emotions (e.g., empathy) can be realized at the hardware level [7–12]. Memristive devices have been approved as candidates for affective devices; this opens up the possibility of using memristors to achieve empathic emotion [13,14]. Recently, some researchers reported that a distinct network of brain regions is activated when we experience others’ feelings, referred to herein as the “empathy network”, and they explained that psychological empathy involves “mirror neurons” [15–21]. It is widely known that synapses constitute most of the functions of neural networks. As the fourth fundamental element, memristors have recently been utilized as artificial synapses and neurons in neuromorphic architectures due to their simplicity and power efficiency and have been found to be a promising candidate for artificial synapses and neurons [12,22–27]. Additionally, more reports have proven that

emerging two-dimensional (2D) layered materials are being actively and innovatively used in memristive devices to make a more intelligent electronic synapse [28–33]. Y. Gogotsi et al. discovered that MXenes have catalyzed the development of a vast and rapidly growing array of 2D materials [34–36]. MXenes, an innovative group of 2D materials, were reported in 2011 [37,38]; they have a high electrical conductivity and show promise in electrical energy storage, electromagnetic interference shielding, electrocatalysis, plasmonics, and other applications [39–42]. Recently, X. Yan et al. reported that 2D MXene (Ti_3C_2) flakes have excellent potential for use in memristor devices, which may open the door for more functions and applications [43]. J. H. Park et al. engineered MXene memristors ($\text{Ti}_3\text{C}_2\text{T}_x$) to improve memory windows and low-power operations through surface modification [44–46]. From this view, 2D-material-based memristors have enormous potential for mimicking empathic affection, which is also an important question for the transition from autistic to empathic artificial intelligence (AI).

In this work, we demonstrated the use of fundamental elements (i.e., an MXene (Ti_3C_2) memristor) to emulate a psychological model of “empathic blame”. A traditional semiconductor process (i.e., physical vapor deposition) based on a silicon substrate was chosen for the process. In a hybrid novel 2D-material-based memristor, the stack of MXene serves as the resistive layer. The integration of MXene was designed to fabricate a conductive filament (CF) between the anode and cathode, which mimics the neurotransmission of biological synapses. MXene was introduced into memristive devices fabricated by mechanical coating. The memristor in our work consisted of a layered device structure including a couple of electrodes, a Cu active layer, and a stack of thin-film MXene (Ti_3C_2). The layered MXene provides metal ion accommodation between the 2D layers and is noted for its chemical and structural variability and surface chemistry tenability. As a result, the layered MXene enabled outstanding and brain-inspired performance in the device. For example, the ultralow threshold voltage of the device was approximately 0.50 V under a direct current (DC) voltage sweeping mode. In addition, analog behavior was reliably presented after programming a DC stimulation. The leaky integrate-and-fire (LIF) model was realized using a single MXene memristor, which consisted of integration, fire, refractory period, and relaxation. Moreover, research on “empathic blame” shows that participants scoring high on dispositional empathic concern (positively correlated with empathic capability) judge intentional harm to be less morally permissible [2]. For our device, we applied a series of identical programming pulses, and the subsequent stimulation required fewer pulses to reach the corresponding weights. We demonstrated that the experimental sequence fit the value of empathic concern in the empathy model. For instance, the second stimulation had more experience with the responsive weight than the first stimulation, which determined a stronger empathic capability. Meanwhile, the necessary number of pulses for the rated weight corresponded to the moral permissibility score. As a result, compared with the empathic–emotional investigation, a memristive device with films of MXene was highly relevant to the moral-permissible function of “empathic blame”. This particular property gives great convenience to the design of artificial neural systems with rich emotional capabilities. According to the neural basis of empathy, we designed a third-party judgment system that can continuously simulate high, medium, and low levels of empathy. This work not only expands the applications of MXene to new neuromorphic areas but also provides memristive devices with a corresponding type of empathic emotion in our system, which may equip AI with an accurate and rich emotional capability at the hardware level.

2. Materials and Methods

The Cu/MXene (Ti_3C_2)/Cu memristor was fabricated on a Si wafer. From the bottom up, the structure of the Cu/MXene (Ti_3C_2)/Cu memristor consisted of a bottom Cu electrode (80 nm), an active layer (MXene), and a top Cu electrode (100 nm). The metallic Cu layer was deposited via direct current (DC) sputtering at room temperature. Additionally, MXene was prepared by etching Ti_3AlC_2 with hydrofluoric acid (HF). MXene (Ti_3C_2) was

prepared by etching Ti_3AlC_2 with LiF and HCl. The raw material Ti_3AlC_2 was purchased from Laizhou Kai Kai Ceramic Materials Co., Ltd. (Laizhou, China). Generally, 2 g of the Ti_3AlC_2 powders was dispersed in 20 mL of a 6 M HCl aqueous solution containing 1.98 g of LiF. The mixture was magnetically stirred for 24 h at 35 °C. The resulting suspension was washed multiple times with deionized water until a pH above 6 was reached. Finally, Ti_3C_2 powders were obtained via centrifugation and vacuum drying. For the production of few-layer Ti_3C_2 nanosheets, 1 g of the dried Ti_3C_2 multilayer powders was dispersed in 100 mL of distilled water. After four hours of sonication under an argon atmosphere, the suspension was then centrifuged for 60 min at 3500 rpm. Few-layer Ti_3C_2 nanosheets were obtained by vacuum filtration of the resulting supernatant and vacuum drying. Then, the obtained Ti_3C_2 powder was distributed into deionized water at a ratio of 1:30. We used a spin coater for the fabrication of a uniform few-layer Ti_3C_2 film at 3500 rpm for 180 s. Finally, the top Cu electrode was deposited with a thickness of 100 nm by magnetron sputtering using a hard mask. The shape of the top Cu electrode in single device was a square with a side length of 500 μm .

After the fabrication, scanning electron microscopy (SEM) was performed using an FEI Nova NanoSEM 450 scanning electron microscope from Hillsboro, OR, USA. Powder X-ray diffraction (XRD) patterns of the samples were acquired using a Philips X'Pert X-ray diffractometer from Amsterdam, The Netherlands. All of the electrical characteristics were measured by a Keithley 4200A-SCS semiconductor analyzer from Solon, OH, USA.

3. Results and Discussion

Figure 1a shows the atomic structure of the fabricated MXene designed by 3ds Max, which clearly shows the distribution of carbon and titanium atoms. After the ultrasonic dispersion process, the prepared MXene continued to stratify, resulting in distinctive surface characteristics. The SEM images (Figure 1b) vividly illustrate the ultrathin morphology of the layered MXene following the exfoliation process. Additionally, the TEM image shows the single- or several-layer MXene, demonstrating the two-dimensional (2D) structure of lamellar Ti_3C_2 . Initially, a processed uniform layer of MXene film constitutes the foundation of high-performance nanoelectronic devices. Figure 1d shows the XRD pattern of Ti_3C_2 . Compared with the phase of the precursor Ti_3AlC_2 , the absence of the strongest peak and the emergence of a broader (002) peak indicate the successful etching of aluminum from the Ti_3AlC_2 phase after the HF treatment based on the process of MXene fabrication; thus, the desired $\text{Ti}_3\text{C}_2\text{T}_x$ was obtained.

Figure 2a illustrates the schematic layout of the measurement configuration of the device. Throughout the electrical tests, a voltage bias was applied to the Cu top electrode, while the Cu bottom electrode remained grounded. Under the direct current (DC)-programmed biasing conditions, distinct threshold switching characteristics were observed. Figure 2b plots the typical hysteretic I - V characteristic curves on linear scales. The insert figure describes the relationship between sweeping voltage and time. The voltage step and time interval were set to 2.0 mV and 10 ms, respectively. The direction of the programmed sweeping voltage is illustrated in Figure 2b, and is delineated by the numerical sequence of 1~6. To safeguard the devices from irreversible breakdown, a current compliance (CC) of 1.0 μA was employed. During the positive voltage sweep processes 1 and 2 (i.e., 0 to 0.6 V), the conductance exhibited a gradual increase followed by a sudden transition from a high-resistance state (HRS) (OFF state) to a low-resistance state (LRS) (ON state) at a threshold voltage of approximately 0.48 V. As the following process 3 (i.e., 0.6 to 0 V) progressed, the current decreased abruptly from the CC (1 μA) to a low conductivity at a hold voltage of \sim 0.29 V. Subsequently, upon completion of the sweeping processes 4, 5, and 6, the memristor exhibited a symmetric switching behavior under both negative and positive voltage biases. Processes 4 and 5 increased the current repeatedly, similar to a positive-V bias. However, the absolute value of the threshold voltage was \sim -0.45 V. Then, as the device underwent the last sweep process 6 (i.e., -0.6 V to 0 V), the conductance decreased uniformly to the original electronic state before the measurement, exhibiting volatile switching char-

acteristics. The DC-programmed threshold switching hysteretic I - V curve was smooth and did not exhibit any abrupt waves in the conductance. Therefore, such memristors have the potential to achieve analog switching. In this Cu/MXene/Cu device, the low operating voltage of ~ 0.50 V amounts to ultralow power consumption and contributes to the realization of high-density memristor applications. MXene (Ti_3C_2) plays a pivotal role in enhancing the conductivity of this device, leading to its remarkable performance in terms of low power consumption. The mechanism of the threshold switching behavior can be elucidated through ion migration-based filamentary processes. Specifically, under a positive voltage bias, the oxidation and migration of Cu atoms from the top electrode into the MXene flakes are facilitated by defects within the MXene flakes, thereby contributing to filament formation. Conversely, when subjected to a negative voltage bias, Cu atoms undergo similar oxidation and migration processes from the top electrode into the MXene flakes.

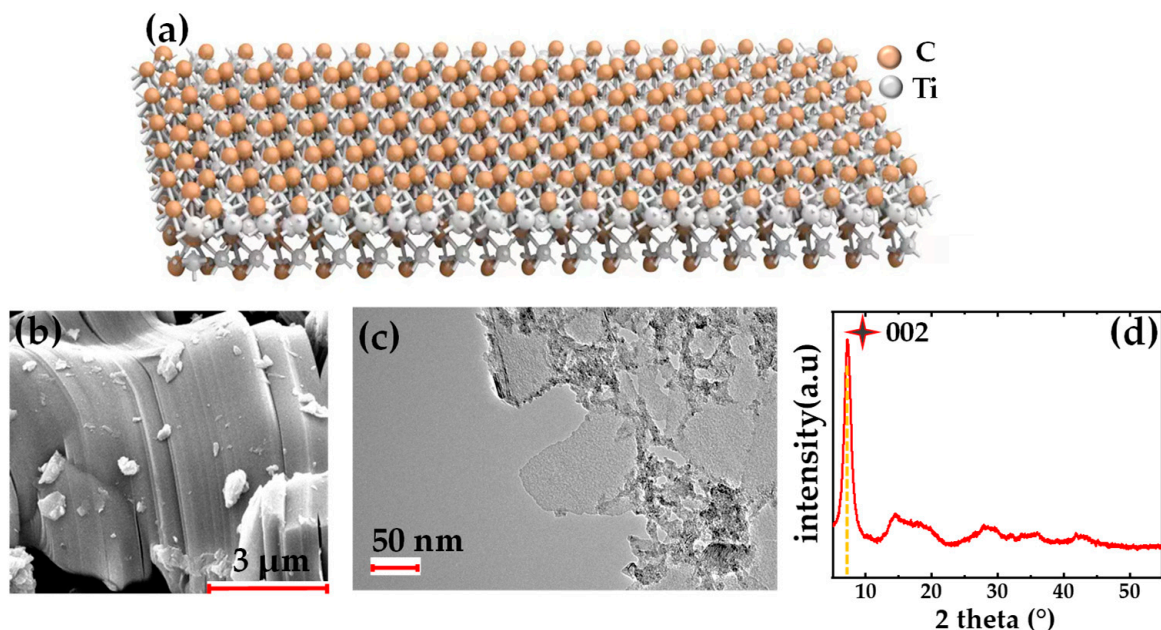


Figure 1. Physical representations of the materials. (a) The atomic structural model of MXene. (b) Scanning electron microscopy (SEM) image of the prepared single- and few-layer MXenes after ultrasonic dispersion treatment. (c) Transmission electron microscope (TEM) image of the Ti_3C_2 . (d) Powder X-ray diffraction (XRD) patterns of samples (red line), where in yellow line represents the (002) peak.

Based on the hysteretic I - V curves, we successfully engineered a Cu/MXene/Cu memristor that demonstrates analog switching behavior during standard voltage sweep conditions. As shown in Figure 2c, on a linear scale, the programmed voltage sweeps increased from zero to 0.1 V (increasing by 0.1 V from 0.1 V to 0.5 V) and then decreased back to zero. During the switching cycle (0.1 V to 0.5 V), a train of programmed sweeps was applied to incrementally increase the device conductance, which showed a more than 100 times higher current than the initial state. However, an obvious window was not observed in the analog curves within the sweeping voltage, which ranged from 0.1 V to 0.5 V. Figure 2d plots the whole train of the sweeping program on semilogarithmic scales. The presence of the MXene film sandwiched between the two electrodes contributed to the wide resistive switching window observed in the device. Upon application of the 0.6 V programmed sweep, the device demonstrated a threshold switching curve, depicted by the red line in Figure 2d. The total analog switching process is plotted in the insert in Figure 2c, wherein the switching rate was approximately 83 mV/s. The retention at 0.02 V after the 1.0 V voltage switch is plotted in the insert in Figure 2d. It is obvious that the LRS of the

device returned to the initial resistance state (HRS) after a period of 20 s. As a result, this device showed volatile threshold switching characteristics, ranging from 1 to 10 μA (CC).

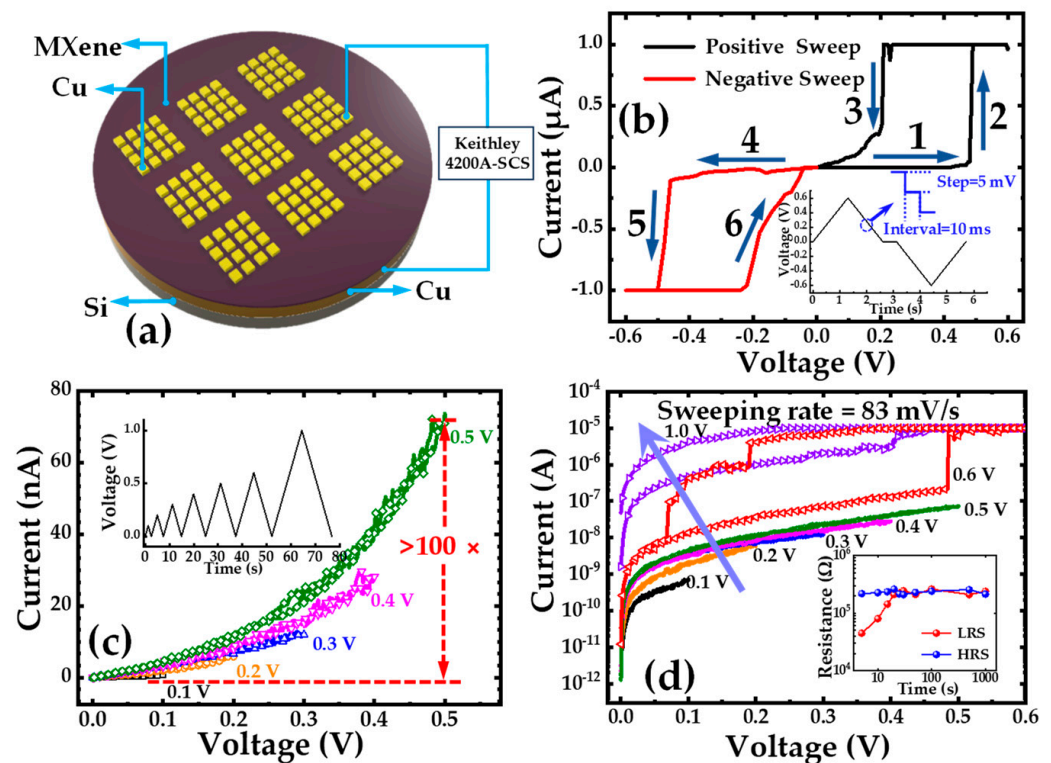


Figure 2. DC I - V curves of the Cu/MXene/Cu memristor. (a) Schematic of configuration of the device. (b) The symmetrical DC-programmed I - sV curves of the threshold switching Cu/MXene/Cu memristor with a step of 5 mV and an interval of 10 ms. (c,d) I - V characteristics of the memristor for increasing positive bias voltages with a step of 2 mV and an interval of 24 ms, wherein the purple arrow describes the trend of analog. The sweeping rate of this series was approximately 83 mV/s. The retention test is shown in the insert in (d).

The I - V characteristic curve illustrates the volatile switching behavior under a series of voltage sweeps for the MXene memristor, demonstrating analog programmed switching behavior. This behavior entails the gradual modulation of the device conductance, indicating its potential for “empathic simulation”. In other words, the device exhibited the ability to adjust its conductance in response to varying input stimuli, akin to the dynamic modulation observed in empathic processes. This analog switching behavior suggests the capability of the MXene memristor to simulate empathic responses, offering promising avenues for applications in neuromorphic computing and artificial intelligence.

The leaky integrate-and-fire neuron model is a typical and simple neural model for neuromorphic units. To explore the neuromorphic behaviors of the device, we implemented the leaky integrate-and-fire (LIF) neuron, as illustrated in Figure 3a. The device was subjected to a series of input pulses characterized by an amplitude of 1.0 V and a width of 30 ms (depicted as gray square waves). Throughout this process, the device exhibited distinct stages, including integration (represented in black), firing (highlighted in red), a refractory period (depicted in green), and relaxation (illustrated in blue). Remarkably, as the input pulses accumulated over a duration of 1.0 s, the conductivity of the device surged from 0.09 μS to 8.1 μS , indicating the initiation of the firing process. This firing process bears similarities to the volatile threshold switching behavior observed in DC tests, underscoring the capability of MXene memristors to emulate neuromorphic functionalities.

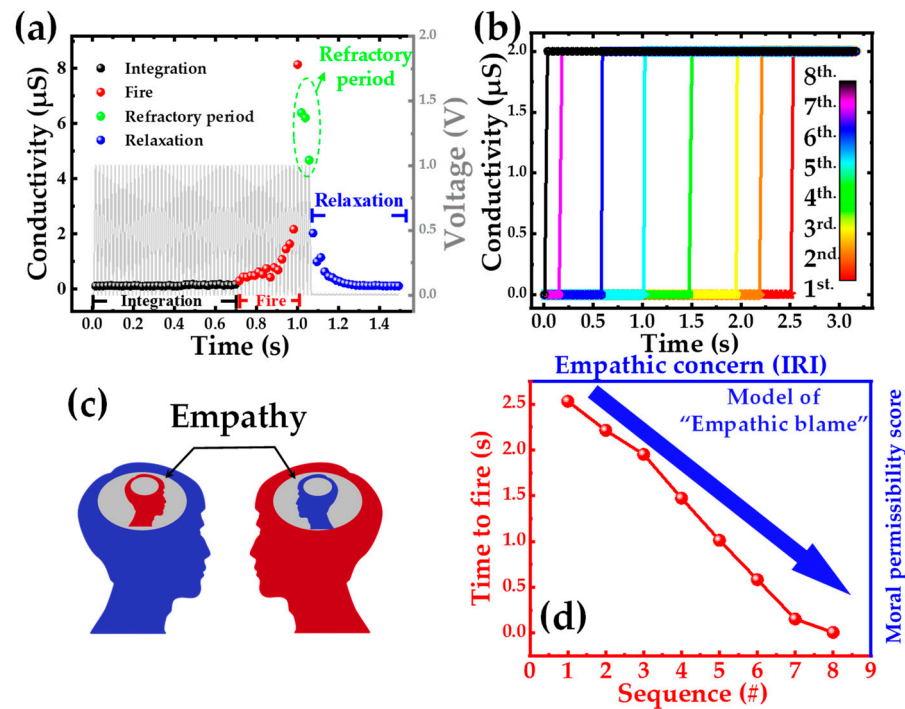


Figure 3. Pulse responses and emulation of empathic blame model using the Cu/MXene/Cu memristor. (a) Leaky integrate-and-fire (LIF) neuron model. (b) Conductivity–time curves with the same set pulse voltage at 1.0 V (30 ms) and read pulse voltage at 0.01 V (10 ms) in the ordered sequence. (c) Schematic of the empathy model. (d) Empathic concern (EC) subscale of the Interpersonal Reactivity Index (IRI). The relationship between time to fire and the testing sequence.

Following the process of neuronal firing, a refractory period ensued, as indicated by the green points in the graph. During this refractory period, which mimics the behavior of biological neurons, the post-neuron temporarily lost its ability to spike again for a specific duration. This temporal pause allows the membrane potential of neurons to recover and reset, preparing it to effectively respond to new input stimuli. Subsequently, after this refractory period, a sequence of input pulses was replaced by reading pulses (0.01 V, 30 ms), prompting the device to transition back to its initial state, known as relaxation (blue). This process of relaxation matches the mechanism of the device, wherein Cu ions diffuse back to the electrode under read pulses or no bias because of interfacial energy minimization. These characteristics closely resemble the neural activity observed in human brain neurons, highlighting the capacity of the MXene device to emulate biological processes.

On the basis of the LIF model, we demonstrated the threshold self-adaptive behavior of neurons. As depicted in Figure 3b, the LIF curves from the first (red) to the eighth (black) stimulation demonstrate that with each successive stimulation on the same device, the integration time (time to firing) of the subsequent sequence decreased in comparison to the preceding sequence. This implies that the subsequent testing sequence will exhibit a lower firing threshold compared to the preceding testing sequence, demonstrating a form of threshold self-adaptive behavior. To elucidate the phenomenon of this threshold self-adaptive behavior, we surmised that the presence of residual Cu atoms may facilitate subsequent firing processes. This suggests that the residual Cu atoms could potentially contribute to the adaptability of the threshold behavior.

With regard to Indrajeet Patil’s research focused on the role of empathy for the victim of a harmful act, the pulse response curves fit the behavior of “empathic blame” [2]. Specifically, the “empathic blame” hypothesis suggests that the extent to which we criticize others for causing harmful outcomes, whether intentional or unintentional, is contingent upon our level of empathy with the victim’s suffering (Figure 3c). As shown in Figure 3d, people with a higher level of empathy show a lower moral permissibility for people who caused

harmful outcomes. In essence, individuals with high dispositional EC tended to perceive intentional harm as less morally permissible. In our progress, the more the device experienced, the less time it took to fire. Devices subjected to higher levels of stimulation showed diminished integration permissibility and an elevated likelihood of emission, akin to the phenomenon of “empathic blame”.

Equipped with different levels of empathy, people do not necessarily make an indistinguishable moral judgment for the same action. In this work, based on the biological neural mechanism of empathy, we designed a moral judgment reasoning system. As shown in Figure 4a, the system maps the empathy index $E(x)$ to the judgment result $J(x)$ under the evolution of the neural network. Then, the system will evolve a moral judgment of the issues that people (i.e., Tom) created. The whole system consists of an empathy network, an assessment network, and an integrative network that imitates the dorsolateral prefrontal cortex (dlPFC) [47]. The dlPFC functions as a comprehensive, integration network within the decision-making system. It amalgamates representations of inputs from various subprocesses to influence the selection of responses [48]. After receiving external information, the empathy network encodes representations of harmful outcomes, and the evaluation neural network encodes representations of the intentions and results. Finally, the integrative network selects and integrates the above three types of representations on the basis of a moral judgment (i.e., acceptance or blame).

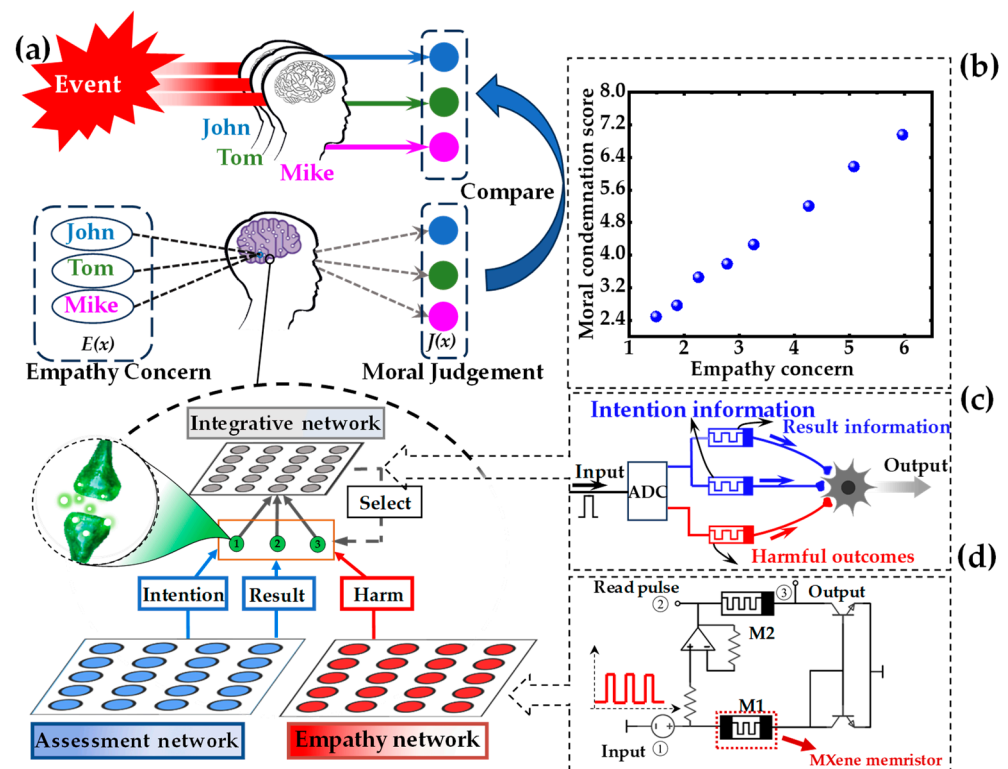


Figure 4. Diagram of an artificial neural system for empathic moral judgment. (a) Schematic architecture of a moral blame judgment model. (b) Results for this model. (c) Schematic of the analog-to-digital converter (ADC) in the integrative network. (d) Circuit diagram of the empathy network.

Figure 4d shows the implementation of the “empathy network” circuit. As the potential core in biological empathy, mirror neurons are ingeniously emulated in this circuit. In this circuit, the MXene memristor was selected as element M1 because of its empathic capability, and a charge-controlled memristor (i.e., HP memristor) was chosen as M2. To mimic the biological stimulus signals an empathy network receives, a series of consecutive identical voltage pulses was input to port 1 in the circuit. M1 with different empathy abilities will generate current signals of different sequences inspired by the stimulus signals

with the same sequence. All these current signals will be transmitted to M2, controlled by the mirror current source. Then, the final encoded value will also be exported as the resistance value of M2, which is also the encoded value of the empathy network. The same intention information and encoded value of the harmful result will be shown in the form of the resistance value of the charged memristor. After the coding process, by inputting a read pulse to port 2, we can obtain the final encoding value of the empathy network according to the export current in port 3.

Figure 4c illustrates a schematic diagram of the selection and integration functions of the integrative network. Based on different types of moral judgments, the integrative network inputs programming pulses to the analog-to-digital converter (ADC), and the ADC converts the programming pulses into an appropriate read pulse vector to selectively read them out. The ADC mimics varying degrees of coupling with the integrative network and other networks, including an empathy network and an assessment network. The current of the encoded value is then integrated into the decision-making neurons in the integrated network to complete the system's reasoning of the moral judgment results.

Within this conceptual framework, we delved into the nuances of moral judgments directed at individuals, such as John, Tom, and Mike, each exhibiting distinct empathic responses to unintentional injury scenarios. Given the inherent nature of such incidents, where injuries are unintentional, the intention memristor assumes a high-resistance state, while the injury memristor adopts a low-resistance state. The analog-to-digital converter (ADC) inputs programming pulses, exemplified by a 3 V square wave with a duration of 1.0 ms, to facilitate the system's attributions of blame. The calculated energy consumption of this intricate circuitry amounted to 244.8 μJ , underscoring its efficiency within the computational domain.

Figure 4b depicts the reasoning results for the blame judgment; people with a greater empathic capability output more blame judgments. Compared to the experiment on "empathic blame", this trend is consistent with psychological facts.

In fact, the human brain does not always strictly process signals according to physical laws and mathematical equations. In the test, the decision simulates a simple nerve cell with three inputs and outputs. If the neural network is designed to be more complicated, the system will make a perfect judgment. Aggregating such rich human emotion information into a more advanced brain-inspired decision-making system is expected to pave the way for achieving a vivid, deep emotional interaction between AI and human beings at the hardware level.

4. Conclusions

In this work, we achieved a pioneering human-like affective model of "empathic blame" using an MXene memristor. First, we introduced MXene into a memristive device, serving as a resistive switching layer. Specifically, due to MXene, the threshold switching behavior of the memristor was investigated during an applied DC stimulation, which included vivid analog behavior and quaternary states of multiple resistances. It is obvious that the DC voltage results initially exhibited the potential to realize brain-inspired behaviors. Moreover, the implementation of the LIF model was achieved utilizing a single MXene memristor, encompassing the phases of integration, firing, a refractory period, and relaxation. As a result, this device shows self-adaptive characteristics in the time of integration to fire. In addition, drawing from the "empathic blame" hypothesis, which links our condemnation of others for causing harm to our level of empathy with the victim's suffering, we individualized the hypothesis into our MXene memristor. Concretely, the permissible time required to reach the fixed weight was compared to the permission time for others to produce harmful outcomes. As a result, our MXene memristor could respond to a fixed weight empathically within sequential rehearsals. Furthermore, considering that the ADC can also be realized by a Hopfield neural network consisting of memristors, the artificial neural system designed in the experiment reveals the possibility of using memristors with various properties to construct a brain-inspired system [49–51]. Additionally, we will

try to strength the emulation of mirror neurons and prepare demonstrations of an empathic blame system through physical representations based on MXene memristors. However, the human brain does not always adhere strictly to physical laws and mathematical equations. For affective computing and brain-inspired computing systems, this hardware design may pave the way for the realization of empathic AI.

Author Contributions: Y.W. (Yu Wang) and Y.Z. fabricated the devices. Y.W. (Yu Wang) and Y.W. (Yanji Wang) designed and conducted all the experiments and analyzed the data. Y.Z. and Y.W. (Yu Wang) performed the material characterization. Y.T. and R.X. planned and supervised the whole project. All authors contributed to discussing the results and the manuscript revisions. All authors have read and agreed to the published version of the manuscript.

Funding: This research was funded by the 2030 Major Project of the Chinese Ministry of Science and Technology, grant number 2021ZD0201200.

Data Availability Statement: The data presented in this study are available on request from the corresponding author.

Acknowledgments: We thank Yihao Chen for support in the circuit design.

Conflicts of Interest: The authors declare no conflicts of interest.

References

1. Cuff, B.M.; Brown, S.J.; Taylor, L.; Howat, D.J. Empathy: A review of the concept. *Emot. Rev.* **2016**, *8*, 144–153. [[CrossRef](#)]
2. Patil, I.; Calò, M.; Fornasier, F.; Cushman, F.; Silani, G. The behavioral and neural basis of empathic blame. *Sci. Rep.* **2017**, *7*, 5200. [[CrossRef](#)]
3. Decety, J.; Echols, S.; Correll, J. The blame game: The effect of responsibility and social stigma on empathy for pain. *J. Cognit. Neurosci.* **2010**, *22*, 985–997. [[CrossRef](#)] [[PubMed](#)]
4. Crisan, S.; Canache, M.; Buksa, D.; Nechita, D. A comparison between self-compassion and unconditional self-acceptance: Interventions on self-blame, empathy, shame-, guilt-proneness, and performance. *J. Ration.-Emotive Cogn.-Behav. Ther.* **2023**, *41*, 64–80. [[CrossRef](#)]
5. Maharani, F.; Adiningrum, R.; Mohammad, W. Character AI Personas' Views on User's Psychological Sin Statements and Self-Blame. *Arika J. Digit. Mark. Consum. Behav.* **2023**, *1*, 1–8.
6. Walkington, Z.; Wigman, S.A.; Bowles, D. The impact of narratives and transportation on empathic responding. *Poetics* **2020**, *80*, 101425. [[CrossRef](#)]
7. Ji, X.; Dong, Z.; Han, Y.; Lai, C.S.; Qi, D. A brain-inspired hierarchical interactive in-memory computing system and its application in video sentiment analysis. *IEEE Trans. Circuits Syst. Video Technol.* **2023**, *33*, 7928–7942. [[CrossRef](#)]
8. Ji, X.; Dong, Z.; Lai, C.S.; Qi, D. A brain-inspired in-memory computing system for neuronal communication via memristive circuits. *IEEE Commun. Mag.* **2022**, *60*, 100–106. [[CrossRef](#)]
9. Dong, Z.; Ji, X.; Wang, J.; Gu, Y.; Wang, J.; Qi, D. ICNCS: Internal cascaded neuromorphic computing system for fast electric vehicle state of charge estimation. *IEEE Trans. Consum. Electron.* **2023**. [[CrossRef](#)]
10. Dong, Z.; Ji, X.; Lai, C.S.; Qi, D. Design and implementation of a flexible neuromorphic computing system for affective communication via memristive circuits. *IEEE Commun. Mag.* **2022**, *61*, 74–80. [[CrossRef](#)]
11. Ji, X.; Dong, Z.; Han, Y.; Lai, C.S.; Zhou, G.; Qi, D. EMSN: An energy-efficient memristive sequencer network for human emotion classification in mental health monitoring. *IEEE Trans. Consum. Electron.* **2023**, *69*, 1005–1016. [[CrossRef](#)]
12. Ji, X.; Lai, C.S.; Zhou, G.; Dong, Z.; Qi, D.; Lai, L.L. A flexible memristor model with electronic resistive switching memory behavior and its application in spiking neural network. *IEEE Trans. Nanobiosci.* **2022**, *22*, 52–62. [[CrossRef](#)]
13. Dong, Z.; Ji, X.; Lai, C.S.; Qi, D.; Zhou, G.; Lai, L.L. Memristor-based hierarchical attention network for multimodal affective computing in mental health monitoring. *IEEE Consum. Electron. Mag.* **2022**, *12*, 94–106. [[CrossRef](#)]
14. Ji, X.; Dong, Z.; Lai, C.; Zhou, G.; Qi, D. A physics-oriented memristor model with the coexistence of NDR effect and RS memory behavior for bio-inspired computing. *Mater. Today Adv.* **2022**, *16*, 100293. [[CrossRef](#)]
15. Keysers, C. Mirror neurons. *Curr. Biol.* **2009**, *19*, R971–R973. [[CrossRef](#)] [[PubMed](#)]
16. Iacoboni, M. Imitation, empathy, and mirror neurons. *Annu. Rev. Psychol.* **2009**, *60*, 653–670. [[CrossRef](#)]
17. Plata-Bello, J.; Privato, N.; Modroño, C.; Pérez-Martín, Y.; Borges, Á.; González-Mora, J.L. Empathy Modulates the Activity of the Sensorimotor Mirror Neuron System during Pain Observation. *Behav. Sci.* **2023**, *13*, 947. [[CrossRef](#)] [[PubMed](#)]
18. Kilner, J.M.; Lemon, R.N. What we know currently about mirror neurons. *Curr. Biol.* **2013**, *23*, R1057–R1062. [[CrossRef](#)] [[PubMed](#)]
19. Heyes, C.; Catmur, C. What happened to mirror neurons? *Perspect. Psychol. Sci.* **2022**, *17*, 153–168. [[CrossRef](#)]
20. Oztop, E.; Kawato, M.; Arbib, M.A. Mirror neurons: Functions, mechanisms and models. *Neurosci. Lett.* **2013**, *540*, 43–55. [[CrossRef](#)]
21. Miall, R.C. Connecting mirror neurons and forward models. *Neuroreport* **2003**, *14*, 2135–2137. [[CrossRef](#)] [[PubMed](#)]

22. Strukov, D.B.; Snider, G.S.; Stewart, D.R.; Williams, R.S. The missing memristor found. *Nature* **2008**, *453*, 80–83. [[CrossRef](#)]
23. Wang, Z.; Joshi, S.; Savel'ev, S.E.; Jiang, H.; Midya, R.; Lin, P.; Hu, M.; Ge, N.; Strachan, J.P.; Li, Z. Memristors with diffusive dynamics as synaptic emulators for neuromorphic computing. *Nat. Mater.* **2017**, *16*, 101–108. [[CrossRef](#)] [[PubMed](#)]
24. Yoon, J.H.; Wang, Z.; Kim, K.M.; Wu, H.; Ravichandran, V.; Xia, Q.; Hwang, C.S.; Yang, J.J. An artificial nociceptor based on a diffusive memristor. *Nat. Commun.* **2018**, *9*, 417. [[CrossRef](#)]
25. Yao, P.; Wu, H.; Gao, B.; Tang, J.; Zhang, Q.; Zhang, W.; Yang, J.J.; Qian, H. Fully hardware-implemented memristor convolutional neural network. *Nature* **2020**, *577*, 641–646. [[CrossRef](#)] [[PubMed](#)]
26. Jo, S.H.; Chang, T.; Ebong, I.; Bhadviya, B.B.; Mazumder, P.; Lu, W. Nanoscale memristor device as synapse in neuromorphic systems. *Nano Lett.* **2010**, *10*, 1297–1301. [[CrossRef](#)]
27. Xu, Z.; Li, Y.; Xia, Y.; Shi, C.; Chen, S.; Ma, C.; Zhang, C.; Li, Y. Organic Frameworks Memristor: An Emerging Candidate for Data Storage, Artificial Synapse, and Neuromorphic Device. *Adv. Funct. Mater.* **2024**, *34*, 2312658. [[CrossRef](#)]
28. Huh, W.; Lee, D.; Lee, C.H. Memristors based on 2D materials as an artificial synapse for neuromorphic electronics. *Adv. Mater.* **2020**, *32*, 2002092. [[CrossRef](#)] [[PubMed](#)]
29. Wang, M.; Cai, S.; Pan, C.; Wang, C.; Lian, X.; Zhuo, Y.; Xu, K.; Cao, T.; Pan, X.; Wang, B. Robust memristors based on layered two-dimensional materials. *Nat. Electron.* **2018**, *1*, 130–136. [[CrossRef](#)]
30. Teja Nibhanupudi, S.; Roy, A.; Veksler, D.; Coupin, M.; Matthews, K.C.; Disiena, M.; Ansh; Singh, J.V.; Gearba-Dolocan, I.R.; Warner, J. Ultra-fast switching memristors based on two-dimensional materials. *Nat. Commun.* **2024**, *15*, 2334. [[CrossRef](#)]
31. Zhu, K.; Pazos, S.; Aguirre, F.; Shen, Y.; Yuan, Y.; Zheng, W.; Alharbi, O.; Villena, M.A.; Fang, B.; Li, X. Hybrid 2D–CMOS microchips for memristive applications. *Nature* **2023**, *618*, 57–62. [[CrossRef](#)] [[PubMed](#)]
32. Li, M.; Liu, H.; Zhao, R.; Yang, F.-S.; Chen, M.; Zhuo, Y.; Zhou, C.; Wang, H.; Lin, Y.-F.; Yang, J.J. Imperfection-enabled memristive switching in van der Waals materials. *Nat. Electron.* **2023**, *6*, 491–505. [[CrossRef](#)]
33. Xie, M.; Jia, Y.; Nie, C.; Liu, Z.; Tang, A.; Fan, S.; Liang, X.; Jiang, L.; He, Z.; Yang, R. Monolithic 3D integration of 2D transistors and vertical RRAMs in 1T–4R structure for high-density memory. *Nat. Commun.* **2023**, *14*, 5952. [[CrossRef](#)] [[PubMed](#)]
34. VahidMohammadi, A.; Rosen, J.; Gogotsi, Y. The world of two-dimensional carbides and nitrides (MXenes). *Science* **2021**, *372*, eabf1581. [[CrossRef](#)] [[PubMed](#)]
35. Gogotsi, Y.; Anasori, B. The rise of MXenes. *ACS Nano* **2019**, *13*, 8491–8494. [[CrossRef](#)] [[PubMed](#)]
36. Gogotsi, Y.; Huang, Q. MXenes: Two-dimensional building blocks for future materials and devices. *ACS Nano* **2021**, *15*, 5775–5780. [[CrossRef](#)]
37. Naguib, M.; Kurtoglu, M.; Presser, V.; Lu, J.; Niu, J.; Heon, M.; Hultman, L.; Gogotsi, Y.; Barsoum, M.W. Two-dimensional nanocrystals: Two-dimensional nanocrystals produced by exfoliation of Ti_3AlC_2 (Adv. Mater. 37/2011). *Adv. Mater.* **2011**, *23*, 4207. [[CrossRef](#)]
38. Naguib, M.; Mashtalir, O.; Carle, J.; Presser, V.; Lu, J.; Hultman, L.; Gogotsi, Y.; Barsoum, M.W. Two-dimensional transition metal carbides. *ACS Nano* **2012**, *6*, 1322–1331. [[CrossRef](#)] [[PubMed](#)]
39. Kumar, J.A.; Prakash, P.; Krithiga, T.; Amarnath, D.J.; Premkumar, J.; Rajamohan, N.; Vasseghian, Y.; Saravanan, P.; Rajasimman, M. Methods of synthesis, characteristics, and environmental applications of MXene: A comprehensive review. *Chemosphere* **2022**, *286*, 131607. [[CrossRef](#)]
40. Zhan, X.; Si, C.; Zhou, J.; Sun, Z. MXene and MXene-based composites: Synthesis, properties and environment-related applications. *Nanoscale Horiz.* **2020**, *5*, 235–258. [[CrossRef](#)]
41. Nan, J.; Guo, X.; Xiao, J.; Li, X.; Chen, W.; Wu, W.; Liu, H.; Wang, Y.; Wu, M.; Wang, G. Nanoengineering of 2D MXene-based materials for energy storage applications. *Small* **2021**, *17*, 1902085. [[CrossRef](#)] [[PubMed](#)]
42. Pei, Y.; Zhang, X.; Hui, Z.; Zhou, J.; Huang, X.; Sun, G.; Huang, W. $\text{Ti}_3\text{C}_2\text{TX}$ MXene for sensing applications: Recent progress, design principles, and future perspectives. *ACS Nano* **2021**, *15*, 3996–4017. [[CrossRef](#)]
43. Yan, X.; Wang, K.; Zhao, J.; Zhou, Z.; Wang, H.; Wang, J.; Zhang, L.; Li, X.; Xiao, Z.; Zhao, Q. A new memristor with 2D $\text{Ti}_3\text{C}_2\text{T}_x$ MXene flakes as an artificial bio-synapse. *Small* **2019**, *15*, 1900107. [[CrossRef](#)]
44. Mullani, N.B.; Kumbhar, D.D.; Lee, D.H.; Kwon, M.J.; Cho, S.y.; Oh, N.; Kim, E.T.; Dongale, T.D.; Nam, S.Y.; Park, J.H. Surface Modification of a Titanium Carbide MXene Memristor to Enhance Memory Window and Low-Power Operation. *Adv. Funct. Mater.* **2023**, *33*, 2300343. [[CrossRef](#)]
45. Long, Y.; Tao, Y.; Shang, T.; Yang, H.; Sun, Z.; Chen, W.; Yang, Q.H. Roles of metal ions in MXene synthesis, processing and applications: A perspective. *Adv. Sci.* **2022**, *9*, 2200296. [[CrossRef](#)]
46. Li, Q.; Li, Y.; Zeng, W. Preparation and application of 2D MXene-based gas sensors: A review. *Chemosensors* **2021**, *9*, 225. [[CrossRef](#)]
47. Ebisch, S.J.; Scalabrini, A.; Northoff, G.; Mucci, C.; Sergi, M.R.; Saggino, A.; Aquino, A.; Alparone, F.R.; Perrucci, M.G.; Gallese, V. Intrinsic shapes of empathy: Functional brain network topology encodes intersubjective experience and awareness traits. *Brain Sci.* **2022**, *12*, 477. [[CrossRef](#)]
48. Seminowicz, D.A.; Moayed, M. The dorsolateral prefrontal cortex in acute and chronic pain. *J. Pain* **2017**, *18*, 1027–1035. [[CrossRef](#)]
49. Guo, X.; Merrikh-Bayat, F.; Gao, L.; Hoskins, B.D.; Alibart, F.; Linares-Barranco, B.; Theogarajan, L.; Teuscher, C.; Strukov, D.B. Modeling and experimental demonstration of a Hopfield network analog-to-digital converter with hybrid CMOS/memristor circuits. *Front. Neurosci.* **2015**, *9*, 488. [[CrossRef](#)]

50. Danial, L.; Wainstein, N.; Kraus, S.; Kvatinsky, S. Breaking through the speed-power-accuracy tradeoff in ADCs using a memristive neuromorphic architecture. *IEEE Trans. Emerg. Top. Comput. Intell.* **2018**, *2*, 396–409. [[CrossRef](#)]
51. Wang, W.; Li, Z.; Fu, X.; Wang, Y.; Li, Q. Pipelined Memristive Analog-to-Digital Converter With Self-Adaptive Weight Tuning. *IEEE J. Emerg. Sel. Top. Circuits Syst.* **2022**, *12*, 913–921. [[CrossRef](#)]

Disclaimer/Publisher’s Note: The statements, opinions and data contained in all publications are solely those of the individual author(s) and contributor(s) and not of MDPI and/or the editor(s). MDPI and/or the editor(s) disclaim responsibility for any injury to people or property resulting from any ideas, methods, instructions or products referred to in the content.